Editors' Suggestion

Ferrimagnetic Oscillator Magnetometer

John F. Barry,[1,*] Reed A. Irion,[1] Matthew H. Steinecker,[1] Daniel K. Freeman,[1] Jessica J. Kedziora,[1] Reginald G. Wilcox,[1,2] and Danielle A. Braje[1]

[1] *MIT Lincoln Laboratory, Lexington, Massachusetts 02421, USA*

[2] *Massachusetts Institute of Technology, Cambridge, Massachusetts 02139, USA*

(Received 21 April 2022; revised 14 September 2022; accepted 9 January 2023; published 17 April 2023)

Quantum sensors offer unparalleled precision, accuracy, and sensitivity for a variety of measurement applications. We report a compact magnetometer based on a ferrimagnetic sensing element in an oscillator architecture that circumvents challenges common to other quantum sensing approaches such as limited dynamic range, limited bandwidth, and dependence on vacuum, cryogenic, or laser components. The device exhibits a fixed, calibration-free response governed by the electron gyromagnetic ratio. Exchange narrowing in the ferrimagnetic material produces submegahertz transition linewidths despite the high unpaired spin density (approximately 10^{22} cm^{-3}). The magnetometer achieves a minimum sensitivity of 100 fT/$\sqrt{\text{Hz}}$ to ac magnetic fields of unknown phase and a sensitivity below 200 fT/$\sqrt{\text{Hz}}$ over a 1 MHz bandwidth. By encoding magnetic field in frequency rather than amplitude, the device provides a dynamic range in excess of 1 mT. The passive, thermal initialization of the sensor's quantum state requires only a magnetic bias field, greatly reducing power requirements compared to laser-initialized quantum sensors. With additional development, this device promises to be a leading candidate for high-performance magnetometry outside the laboratory, and the oscillator architecture is expected to provide advantages across a wide range of sensing platforms.

DOI: 10.1103/PhysRevApplied.19.044044

I. INTRODUCTION

In recent years, tremendous experimental effort has advanced quantum sensors [1] using unpaired electron spins embedded in solid-state crystals. These solid-state sensors employ electron paramagnetic resonance to achieve measurement precision and accuracy comparable to their atomic counterparts, but with advantages such as smaller sensing volumes, compatibility with a wide range of ambient conditions, and fixed sensing axes provided by a rigid crystal lattice. The most-developed solid-state quantum sensing platform uses negatively charged nitrogen-vacancy centers in diamond as sensitive magnetic field probes [2,3]. Such sensors have been used to detect or image biological targets [4–9], single proteins [10,11], NMR species [12–16], individual spins [17–20], and condensed matter phenomena [21–25].

Though recent efforts have focused on optically active paramagnetic defects [26–30], ferrimagnetic materials offer distinct advantages for quantum sensors. Ferrimagnetic materials provide higher unpaired electron spin densities than their solid-state paramagnetic counterparts [31], for example 10^{22} cm^{-3} versus 10^{16}–10^{19} cm^{-3}, while the strong coupling of the exchange interaction mitigates the dipolar resonance broadening observed in high-defect-density paramagnetic materials [32,33]. Importantly, initialization of ferrimagnetic spins into the desired quantum state requires only a bias magnetic field, without the need for active optical initialization.

Consequently, magnetic sensors employing spin-wave interferometry in ferrimagnetic films [34,35] or ferrimagnetic resonance (FMR) in spheres [36–38] or films [39–42] have been investigated, including demonstrations with pT/$\sqrt{\text{Hz}}$-level sensitivity. Using ferrimagnetic materials, classical sensors such as fluxgates [43–45] and Faraday-rotation-based devices [46,47] have achieved sensitivities down to 40 fT/$\sqrt{\text{Hz}}$ and 10 pT/$\sqrt{\text{Hz}}$, respectively. Additionally, ferrimagnetic materials have long found commercial use in tunable microwave filters [48,49] and oscillators [50–52]. Despite these well-developed commercial technologies however, magnetometry schemes for ferrimagnetic materials have not previously employed a self-sustaining oscillator architecture to encode magnetic fields in the output waveform frequency rather than amplitude [53]. We find this architecture provides crucial advantages in performance, capabilities, and simplicity of a magnetometer device.

Here we report a magnetometer using FMR as the magnetically sensitive frequency discriminator in an electronic oscillator. With this construction, the frequency of the

*john.barry@ll.mit.edu

output voltage signal tracks the FMR frequency, which varies linearly with the applied magnetic field. This ferrimagnetic oscillator magnetometer exhibits a minimum sensitivity of 100 fT/$\sqrt{\text{Hz}}$ to magnetic fields near 100 kHz and sensitivities below 200 fT/$\sqrt{\text{Hz}}$ from 3 kHz to 1 MHz. As the device encodes the measured magnetic field directly in frequency, superior dynamic range is achieved relative to devices employing amplitude encoding. In addition, the sensor head is simple, compact, and uses lower power than existing quantum magnetometers of comparable sensitivity.

II. OSCILLATOR ARCHITECTURE

Quantum sensors based on atomic vapors or electron spins in solid-state crystals operate by localizing resonances which vary with a physical quantity of interest. For example, the ambient magnetic field may be determined by measuring a ferrimagnetic material's uniform precession frequency [54], the paramagnetic resonance frequency of nitrogen vacancies in diamond [55], or the hyperfine resonance frequency of an alkali vapor [56]. Several experimental techniques have been developed for this task, from continuous-wave absorption [27] or dispersion [28,57] measurements to pulsed protocols such as Ramsey [58] or pulsed electron spin resonance [59] schemes. In all these methods, externally generated electromagnetic fields manipulate the spin system, and the resonance location is determined from the system's resulting response.

As an alternative to probing the spin system with external signals, however, an oscillator architecture can be arranged to generate a microwave (MW) signal that directly encodes the spin resonance location. Such an oscillator consists of two main components: a frequency discriminator and a gain element, arranged in a feedback loop.

The frequency discriminator can be constructed by coupling input MW signals to the discriminator's output through the quantum spins. If the discriminator's input and output are each coupled to the quantum spin resonance, but not directly to each other, the resulting frequency discriminator will pass frequencies near the spin resonance ω_y while rejecting all others.

The gain needed can be provided by an ordinary rf amplifier; by amplifying the frequency discriminator's output and returning a fraction of this signal to the discriminator's input, sustained self-oscillation can be realized [60]. Because only frequencies near the spin resonance ω_y are transmitted through the frequency discriminator, the resultant oscillation frequency ω_c closely tracks the spin resonance.

Thus, the oscillator architecture eliminates the need for an external rf source. The limited component count of the oscillator architecture is advantageous for compactness and design simplicity. In addition, the oscillator architecture encodes the spin resonance in frequency, which can offer greater dynamic range and improved linearity compared to amplitude-encoded measurements [61]; dynamic range is particularly important for a magnetometer, where, for example, detection of a 100 fT signal in Earth's 0.1 mT-scale magnetic field requires a dynamic range of 10^9.

For an oscillator to operate at steady state, losses through the frequency discriminator and other elements must be exactly compensated by the amplifier, producing unity gain around the oscillator loop. Additionally, the phase length around the oscillator loop must equal an integer number of wavelengths at the steady-state oscillator output frequency. Together, these requirements constitute the Barkhausen criterion, and with reasonable assumptions the requirements result in Leeson's equation [60,62–64], an empirical model of phase noise amplitude spectral density applicable to a wide range of oscillators. Leeson's equation is given by

$$\mathcal{L}^{1/2}(f_m) = \sqrt{\frac{1}{2}\left[\frac{f_L^2}{f_m^2}+1\right]\left[\frac{f_c}{f_m}+1\right]\left[\frac{Fk_BT}{P_s}\right]}, \quad (1)$$

where $\mathcal{L}^{1/2}(f_m)$ is the single-sideband phase noise amplitude spectral density at offset frequency f_m from the carrier, f_L is the Leeson frequency (equal to the frequency discriminator's loaded half width at half maximum linewidth), f_c is the $1/f$ flicker noise corner [60,62,65], P_s is the input power to the sustaining amplifier, T is the temperature, k_B is Boltzmann's constant, and F is the oscillator's measured wideband noise factor. Roughly, Leeson's equation expresses the phase noise created by amplified white thermal noise (the final bracketed factor), enhanced within the bandwidth of the frequency discriminator via regeneration (the first bracketed factor), and further enhanced by flicker noise below the noise corner of the amplifier (the second bracketed factor). Additional details of oscillator phase noise are discussed in Supplemental Material (SM) Sec. B [66]. In Sec. III we show that the magnetometer's noise floor is proportional to $f_m \times \mathcal{L}^{1/2}(f_m)$, establishing the oscillator's phase noise as the principal determinant of magnetometer sensitivity.

III. FERRIMAGNETIC RESONANCE

The material with the narrowest known ferrimagnetic resonance linewidth and lowest known spin-wave damping is yttrium iron garnet (YIG), a synthetic, insulating crystal ferrimagnet with chemical composition $Y_3Fe_5O_{12}$. Other attractive aspects of YIG are low acoustic damping, less than that of quartz, and well-developed growth processes which yield samples of high crystal quality [67]. Consequently, YIG is the prototypical material for cavity spintronics research, and is used in magnon-cavity coupling experiments [68–73], magneto-acoustic coupling

studies [74,75], hybrid quantum circuits [76,77], and axion searches [57].

In crystallographically perfect YIG, five of every 20 lattice sites, equivalent to one unit formula $Y_3Fe_5O_{12}$, are populated by trivalent iron (Fe^{3+}, electronic spin $S = 5/2$). The five trivalent iron atoms occupy three tetrahedral lattice sites and two octahedral lattice sites. Strong superexchange interactions, mediated by oxygen ions between the iron ions, align the spins of the three tetrahedral Fe^{3+} antiparallel to the two octahedral Fe^{3+} in the absence of thermal excitation. The strong coupling between nearby electronic spins results in collective spin behavior, including resonances between collective spin states which are observed as ferrimagnetic resonances. The strong spin-spin coupling also results in exchange-narrowing of the ferrimagnetic resonances, allowing submegahertz transition linewidths despite the high unpaired spin density of about 10^{22} cm^{-3}. Narrower resonances are desired to achieve better oscillator phase noise performance. Additional relevant properties of YIG are detailed in SM Sec. C [66].

Kittel's formula for the uniform precession frequency of ferromagnetic resonance [54] is

$$\omega_y = \sqrt{[\gamma B_z + (N_y - N_z)\gamma\mu_0 M_z][\gamma B_z + (N_x - N_z)\gamma\mu_0 M_z]},$$

where γ is the electron gyromagnetic ratio; $\mathbf{B} = B_z\hat{z}$ is the applied magnetic field and defines the system's $\hat{z}$ axis; M_z is the magnetization along $\hat{z}$, where M_z is assumed equal to the saturation magnetization M_s with no MW power applied; N_x, N_y, and N_z are the demagnetization factors; and all quantities are in SI units. Demagnetization factors characterize the shape-dependent reduction in internal magnetic field due to the magnetization [78]. For a spherical sample, $N_x = N_y = N_z = 1/3$, and Kittel's formula becomes

$$\omega_y = \gamma B_z. \tag{2}$$

Kittel's formula neglects crystal anisotropy, but such effects can be treated perturbatively if needed, as detailed in SM Sec. L [66].

A ferrimagnetic resonance can be used to implement the frequency discriminator discussed in Sec. II, as shown in Fig. 1. Consider two orthogonal circular coupling loops with a small ferrimagnetic sphere centered at the intersection of the coupling loop axes, as shown in Fig. 1(d). In the presence of an externally applied dc magnetic bias field $\mathbf{B} = B_0\hat{z}$, the magnetic domains within the sample align along $\hat{z}$, producing a net magnetization. A MW drive signal with angular frequency $\omega_d \approx \omega_y$, applied to the input coupling loop, causes the sphere's magnetization to precess about the $\hat{z}$ axis [79], as shown in Fig. 1(a). This precessing magnetization then inductively couples to the output coupling loop, and the transmission scattering parameter S_{21} obeys

$$S_{21} = \frac{\sqrt{\kappa_1\kappa_2}}{i(\omega_d - \omega_y) + (\kappa_0 + \kappa_1 + \kappa_2)/2} e^{-i\pi/2}, \tag{3}$$

where κ_0, κ_1, and κ_2 are the unloaded FMR linewidth, input coupling rate, and output coupling rate, respectively, in angular frequency units (see SM Sec. D [66]), and the $\pi/2$ phase retardation arises from the gyrator action of the ferrimagnetic material. The power transmission $|S_{21}|^2$ exhibits a Lorentzian line-shape, with a maximum at the FMR frequency ω_y and a loaded full-width-at-half-maximum linewidth $\kappa_L \equiv \kappa_0 + \kappa_1 + \kappa_2$.

As discussed above, changes in the external dc magnetic field alter the FMR frequency ω_y and therefore the oscillator output frequency. The FMR frequency also responds to ac magnetic fields; the mechanism by which ac fields alter the magnetometer output waveform is discussed in SM Sec. F [66]. Operationally, ac magnetic fields are encoded as frequency modulation of the oscillator's output waveform. For example, an ac magnetic field with root-mean-square (rms) amplitude $B_{\text{sen}}^{\text{rms}}$ and angular frequency ω_m produces sidebands at $\pm\omega_m$ relative to the oscillator carrier frequency when applied parallel to $\mathbf{B}_0$. These two sidebands each exhibit a carrier-normalized amplitude of

$$s = \frac{\gamma B_{\text{sen}}^{\text{rms}}}{\sqrt{2}\omega_m}. \tag{4}$$

The oscillator magnetometer's sensitivity can then be determined from the sideband amplitude and the measured phase noise $\mathcal{L}^{1/2}(f_m)$, which represents the background against which the sidebands are discerned; see SM Secs. F and G [66]. The expected sensitivity is

$$\eta(f_m) = \frac{\sqrt{2}f_m}{\gamma/(2\pi)}\mathcal{L}^{1/2}(f_m). \tag{5}$$

We note a striking feature of the oscillator magnetometer architecture: assuming the oscillator phase noise is well described by Leeson's equation [Eq. (1)], the signal $s \propto 1/\omega_m = 1/(2\pi f_m)$ and the phase noise amplitude spectral density $\mathcal{L}^{1/2}(f_m)$ are expected to exhibit nearly identical scaling within a range of frequencies between the noise corner f_c and the Leeson frequency f_L. Thus, the sensitivity of the device versus frequency f_m is expected to be approximately flat for $f_c \lesssim f_m \lesssim f_L$, as discussed in SM Sec. G [66].

IV. EXPERIMENTAL SETUP

While all presently commercially available YIG oscillators [80,81] employ a reflection architecture, the device here employs a transmission (feedback) architecture [82–86]. The transmission oscillator is constructed from four

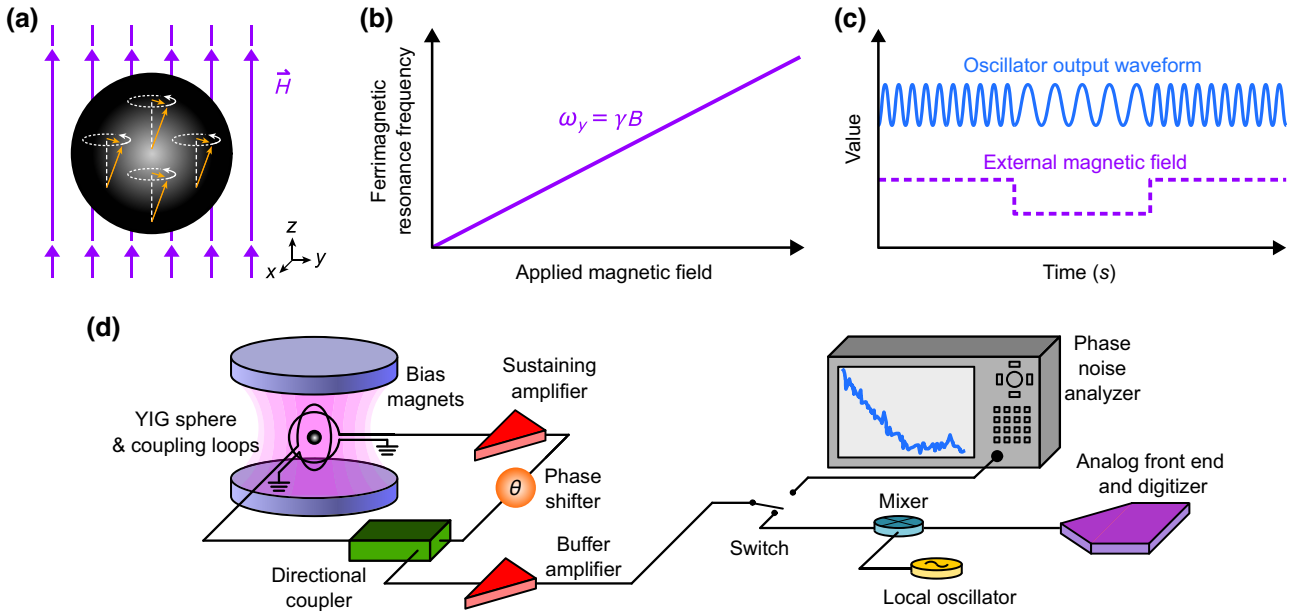

FIG. 1. Oscillator magnetometer principles of operation. (a) In the presence of a uniform external magnetic field, the spins of a ferrimagnetic sphere precess in phase. (b) The resonance frequency of the uniform precession mode varies linearly with applied magnetic field. (c) By using the ferrimagnetic resonance as a frequency discriminator, an oscillator can be constructed where the oscillation frequency tracks the ferrimagnetic resonance frequency. (d) Experimental schematic as described in the main text.

components connected in a serial feedback loop as shown in Fig. 1(d): the FMR frequency discriminator which only passes signals near the ferrimagnetic resonance ω_y, a directional coupler to sample the oscillator waveform for device output, a sustaining amplifier to provide the needed gain, and a mechanical phase shifter to ensure the Barkhausen criterion is satisfied [60].

The device's sensing element is a 1-mm-diameter YIG sphere mounted on the end of an insulating ceramic rod. As shown in Fig. 1, two circular coupling loops in the x-z and y-z planes inductively couple input and output MW signals to the YIG sphere. The coupling loops are mounted orthogonal to each other so that S_{21} transmission occurs only at the FMR frequency and is suppressed elsewhere. The values of κ_0, κ_1, and κ_2 are determined by simultaneously measuring the S-parameters S_{11} and S_{21} of the FMR frequency discriminator using a vector network analyzer; see SM Sec. E [66]. We find $\kappa_0 = 2\pi \times 790$ kHz, $\kappa_1 = 2\pi \times 315$ kHz, and $\kappa_2 = 2\pi \times 405$ kHz. The total loaded linewidth is then $\kappa_L \equiv \kappa_0 + \kappa_1 + \kappa_2 = 2\pi \times 1.510$ MHz, corresponding to a loaded quality factor $Q_L = \omega_y/\kappa_L = 3300$ and a predicted Leeson frequency of $f_L = \frac{1}{2}\kappa_L/(2 \cdot 2\pi) = 755$ kHz.

Two cylindrical permanent magnets positioned symmetrically relative to the YIG sphere create a uniform bias magnetic field $\mathbf{B_0} = B_0\hat{z}$ of approximately 0.178 T, as depicted in Fig. 1. This value of B_0 is more than sufficient to saturate the sphere's magnetization, so that the response is governed by $\omega_y(t) = \gamma B(t)$. The YIG sphere is aligned along the zero temperature compensation axis, as discussed in SM Sec. L [66]. With this bias magnetic field, the oscillation frequency is approximately $2\pi \times 5$ GHz.

The YIG sphere's precessing magnetization continuously induces a sinusoidal voltage on the output coupling loop at the magnetization's precession frequency. This MW voltage signal is first amplified and then mechanically phase-shifted before passing through a 6-dB directional coupler, as shown in Fig. 1(d). The directional coupler's through port directs the MW signal back to the input coupling loop, inductively coupling the MW signal back to the YIG's precessing magnetization and closing the oscillator feedback loop. The mechanical phase shifter is adjusted to minimize the device phase noise, which is measured in real time.

Under operating conditions, the input power to the sustaining amplifier is $P_s \approx 3$ dBm. The sustaining amplifier has a measured gain of 10 dB at $P_s = 3$ dBm so that, after accounting for approximately 2 dB of additional loss, about 11 dBm of MW power is delivered to the input coupling loop. This MW power is estimated to tip the magnetization by approximately 0.1 radians from the z axis; see SM Sec. H [66].

The signal sampled by the 6 dB directional coupler is first amplified by a buffer amplifier and then sent to either a phase noise analyzer for diagnostics and device optimization, or to a mixer which down-converts the signal to an intermediate frequency, ω_i, in the MHz range appropriate for a digitizer. The down-converted signal is demodulated

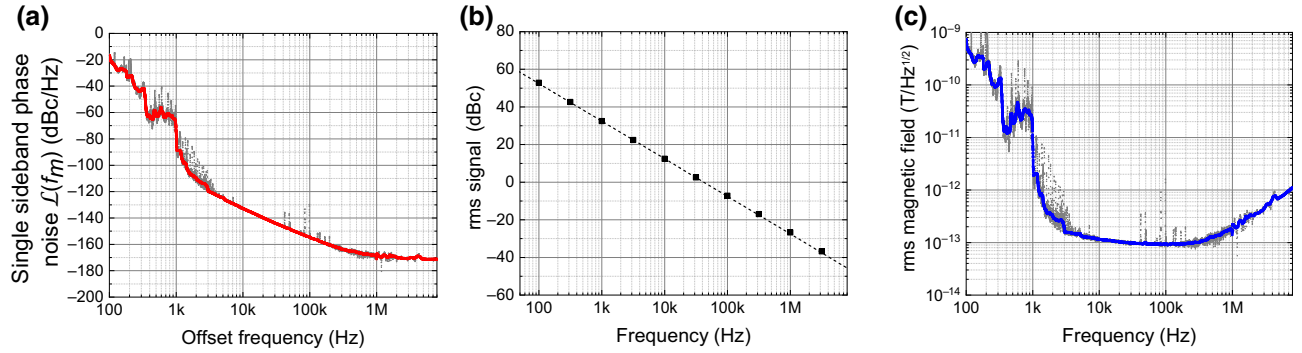

FIG. 2. Performance of the ferrimagnetic oscillator magnetometer. (a) Single-sideband phase noise power spectral density $\mathcal{L}(f_m)$ of the ferrimagnetic oscillator magnetometer. The single-sideband phase noise is −132.8 dBc/Hz and −154.4 dBc/Hz at 10 kHz and 100 kHz offsets from the carrier, respectively. Red depicts smoothed data, while gray depicts the raw phase noise data. (b) Measured response (▪) to a 2.12 μT rms ac magnetic field applied along $\hat{z}$, in agreement with that predicted by Eq. (4) (---). (c) Single-sided magnetic field amplitude spectral density of the ferrimagnetic oscillator magnetometer. The device achieves a minimum sensitivity of approximately 100 fT/$\sqrt{\text{Hz}}$ at frequencies near 100 kHz, with sensitivities below 200 fT/$\sqrt{\text{Hz}}$ from 3 kHz to 1 MHz. Blue depicts smoothed data, while gray depicts the raw data. We note that by convention the single-sideband quantity $\mathcal{L}(f)$ is the positive-frequency half of the double-sided phase noise spectral density, distinct from a single-sided spectrum, which is the sum of positive- and negative-frequency components; see Ref. [87].

to recover the magnetic field time series as described in SM Sec. I [66]. All experiments are performed with the device in an unshielded laboratory environment.

V. EXPERIMENTAL RESULTS

The sensitivity of a magnetometer can be determined from the response to a known applied magnetic field along with the measured noise. As ac magnetic fields are frequency-encoded in the oscillator magnetometer's 5 GHz output waveform, the measured phase noise sets the magnetic sensitivity of the device; see SM Secs. F and G [66]. The oscillator magnetometer's single-sideband phase noise power spectral density $\mathcal{L}(f_m)$ is shown in Fig. 2(a). The device realizes a phase noise of −132.8 dBc/Hz at 10 kHz offset and −154.4 dBc/Hz at 100 kHz offset.

Fitting Leeson's equation [Eq. (1)] to the oscillator's measured phase noise above 3 kHz gives $f_L = 600$ kHz, $F = 8$, and $f_c = 6.6$ kHz with the measured $P_s \approx 3$ dBm. This value of $f_L = 600$ kHz is in reasonable agreement with the value of $f_L = 755$ kHz expected from the FMR frequency discriminator's loaded linewidth.

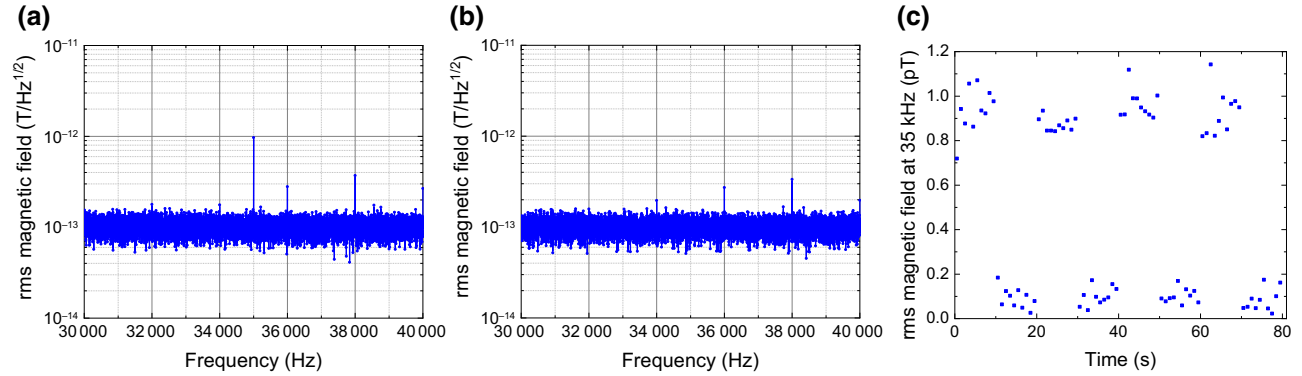

FIG. 3. Magnetometer sensitivity determined from magnetic field time series. (a) Single-sided magnetic field amplitude spectral density in 1-Hz bins with test field $B_{\text{sen}}^{\text{rms}} = 0.9$ pT applied at 35 kHz. The spectrum is obtained by dividing a 10-s magnetic field time series into ten 1-s segments, computing the discrete Fourier transform for each segment, adding components at positive and negative frequencies in quadrature to convert to single-sided spectra, and rms-averaging the ten spectra together. (b) Single-sided magnetic field amplitude spectral density in 1-Hz bins without the test signal applied, obtained as in (a). (c) Value of the 35 kHz frequency bin calculated from 1 s of data per point as the $B_{\text{sen}}^{\text{rms}} = 0.9$ pT signal is chopped on and off. As the device is tested in an unshielded environment, a Tukey window with $\alpha = 0.01$ prevents spectral leakage of low-frequency noise. This window is nearly rectangular, as $\alpha = 0$ and $\alpha = 1$ correspond to rectangular and Hann windows, respectively. The observed 100 fT/$\sqrt{\text{Hz}}$ sensitivity is consistent with that calculated from measured phase noise, shown in Fig. 2(c).

To verify that the device's response matches that predicted by Eq. (4), a sinusoidal magnetic field with rms amplitude $B_{\text{sen}}^{\text{rms}} = 2.12$ μT is applied to the sensor, the angular frequency ω_m of this field is varied, and the carrier-normalized amplitude of the resulting sidebands is recorded. The measured data are in excellent agreement with the theoretical prediction of Eq. (4), as shown in Fig. 2(b).

Having confirmed that the device's frequency response is indeed governed by Eq. (4), the measured phase noise spectrum can be converted to a sensitivity spectrum by Eq. (5), and the result is shown in Fig. 2(c). As discussed previously, the sensitivity is expected to be approximately flat in the region between the amplifier noise corner at $f_c \approx 6.6$ kHz and the Leeson frequency $f_L \approx 600$ kHz. The measured data are consistent with this expectation; for ac signals of unknown phase we observe a minimum sensitivity of approximately 100 fT/$\sqrt{\text{Hz}}$ and a sensitivity below 200 fT/$\sqrt{\text{Hz}}$ over the band from 3 kHz to 1 MHz.

To operate the device as a practical magnetometer, the oscillator output is mixed down and digitized. The magnetic field time series is recovered from the digitized voltage waveform as described in SM Sec. I [66]. To confirm device performance, a 35 kHz sinusoidal test field $B_{\text{sen}}^{\text{rms}} = 0.9$ pT is applied along the sensor's z axis. The resultant amplitude spectral density with the test field on and off is shown in Figs. 3(a) and 3(b) respectively, and a time series of the 35 kHz signal size with the test field chopped on and off is shown in Fig. 3(c). All data are consistent with the expected device response and a minimum sensitivity of 100 fT/$\sqrt{\text{Hz}}$. Supplemental Material Sec. K [66] details calibration of the test field.

VI. DISCUSSION

The device phase noise of −132.8 and −154.4 dBc/Hz at 10 and 100 kHz offset frequencies compares favorably to the lowest-phase-noise commercial YIG oscillators presently available [80,81]. The best commercial device we have measured achieves −112 and −134 dBc/Hz at 10 and 100 kHz from its 5-GHz carrier frequency. The improved performance of our device is likely mainly attributable to a difference in Q_L; whereas we observe $f_L = 600$ kHz $\approx \omega_y/(2\pi \cdot 2Q_L)$, the best commercial oscillator measured exhibits $f_L = 5.2$ MHz. This difference in f_L should translate to an 18.8-dB improvement in phase noise at offset frequencies below f_L, similar to the observed difference of approximately 20 dB.

The device demonstrated here provides the best ac sensitivity achieved to date for a solid-state quantum magnetometer [7,28,88–92]. Among quantum magnetometers, this sensitivity performance is surpassed only by cryogenic superconducting quantum interference device magnetometers and vacuum-based, optically pumped vapor cell magnetometers. Additional sensitivity improvement may be attained by increasing the frequency response to magnetic fields or by decreasing the phase noise. For example, the frequency response could possibly be increased above $\gamma = 2\pi \times 28$ GHz/T in Eq. (2) using strong cavity coupling schemes [28]. Reference [93] describes such a scheme for a ferrimagnetic system with a predicted frequency response of $2\pi \times 500$ GHz/T. Cavity-enhanced ferrimagnetic oscillator magnetometers are currently under investigation and may be explored in future work.

On the other hand, methods to improve oscillator phase noise would also improve sensitivity and are well established. Increasing the sustaining power P_s is a common method to improve oscillator phase noise. However, this approach would likely improve phase noise only at frequencies above the flicker noise corner f_c, and f_c itself may increase with larger values of P_s [60,65]. Further, the maximum usable sustaining power is presently believed to be limited by instabilities arising from nonlinear energy transfer from the uniform precession mode to spin-wave modes [79,94]. Under some conditions not far above current operating powers, we have seen indications that applying additional power to the YIG causes a binary change in the phase noise spectrum of the oscillator, with substantially deteriorated performance.

Other approaches to improving overall phase noise might focus on the amplifier's additive phase noise. Amplifier-induced phase noise can be mitigated using oscillator-narrowing techniques such as Pound-Drever-Hall locking [95–99], carrier suppression interferometric methods [100–105], careful design [106,107] and other approaches [60]. However, even in the ideal case, oscillator-narrowing techniques cannot reduce the oscillator's phase noise to the thermal noise limit of −177 dBm/Hz expected in the absence of Leeson gain. While lowering the Leeson frequency f_L will improve phase noise performance, the noise gain introduced by the Leeson effect appears to be fundamental to the oscillator architecture, as discussed in SM Sec. G [66].

In conclusion, the magnetometer design reported here offers a unique combination of state-of-the-art sensitivity with realistic prospects for improvement, high dynamic range, compactness, and low power requirements. These advantages could drive widespread adoption of similar quantum sensing devices in the near future. The oscillator architecture can be adapted to simplify high-performance ensemble sensing with a range of quantum materials and in a variety of sensing applications, such as sensing of electric fields [108–110], temperature [111], or pressure [112].

ACKNOWLEDGMENTS

The authors acknowledge Peter F. Moulton, Kerry A. Johnson, Liam J. Fitzgerald, and Erik R. Eisenach for helpful discussions. This research was developed with funding

from the Defense Advanced Research Projects Agency and the Under Secretary of Defense for Research and Engineering under Air Force Contract No. FA8702-15-D-0001. The views, opinions, and/or findings expressed are those of the authors and should not be interpreted as representing the official views or policies of the Department of Defense or the U.S. Government. R.A.I. and M.H.S. contributed equally to this work.

[1] C. L. Degen, F. Reinhard, and P. Cappellaro, Quantum sensing, Rev. Mod. Phys. **89**, 035002 (2017).

[2] J. M. Taylor, P. Cappellaro, L. Childress, L. Jiang, D. Budker, P. R. Hemmer, A. Yacoby, R. Walsworth, and M. D. Lukin, High-sensitivity diamond magnetometer with nanoscale resolution, Nat. Phys. **4**, 810 (2008).

[3] C. L. Degen, Scanning magnetic field microscope with a diamond single-spin sensor, Appl. Phys. Lett. **92**, 243111 (2008).

[4] I. Fescenko, A. Laraoui, J. Smits, N. Mosavian, P. Kehayias, J. Seto, L. Bougas, A. Jarmola, and V. M. Acosta, Diamond Magnetic Microscopy of Malarial Hemozoin Nanocrystals, Phys. Rev. Appl. **11**, 034029 (2019).

[5] D. Le Sage, K. Arai, D. R. Glenn, S. J. DeVience, L. M. Pham, L. Rahn-Lee, M. D. Lukin, A. Yacoby, A. Komeili, and R. L. Walsworth, Optical magnetic imaging of living cells, Nature **496**, 486 (2013).

[6] H. C. Davis, P. Ramesh, A. Bhatnagar, A. Lee-Gosselin, J. F. Barry, D. R. Glenn, R. L. Walsworth, and M. G. Shapiro, Mapping the microscale origins of magnetic resonance image contrast with subcellular diamond magnetometry, Nat. Commun. **9**, 131 (2018).

[7] J. F. Barry, M. J. Turner, J. M. Schloss, D. R. Glenn, Y. Song, M. D. Lukin, H. Park, and R. L. Walsworth, Optical magnetic detection of single-neuron action potentials using quantum defects in diamond, Proc. Natl. Acad. Sci. **113**, 14133 (2016).

[8] J. L. Webb, L. Troise, N. W. Hansen, C. Olsson, A. M. Wojciechowski, J. Achard, O. Brinza, R. Staacke, M. Kieschnick, J. Meijer, A. Thielscher, J.-F. Perrier, K. Berg-Sørensen, A. Huck, and U. L. Andersen, Detection of biological signals from a live mammalian muscle using an early stage diamond quantum sensor, Sci. Rep. **11**, 2412 (2021).

[9] K. Arai, A. Kuwahata, D. Nishitani, I. Fujisaki, R. Matsuki, Y. Nishio, Z. Xin, X. Cao, Y. Hatano, S. Onoda, C. Shinei, M. Miyakawa, T. Taniguchi, M. Yamazaki, T. Teraji, T. Ohshima, M. Hatano, M. Sekino, and T. Iwasaki, Millimetre-scale magnetocardiography of living rats with thoracotomy, Commun. Phys. **5**, 200 (2022).

[10] I. Lovchinsky, A. O. Sushkov, E. Urbach, N. P. de Leon, S. Choi, K. De Greve, R. Evans, R. Gertner, E. Bersin, C. Müller, L. McGuinness, F. Jelezko, R. L. Walsworth, H. Park, and M. D. Lukin, Nuclear magnetic resonance detection and spectroscopy of single proteins using quantum logic, Science **351**, 836 (2016).

[11] F. Shi, Q. Zhang, P. Wang, H. Sun, J. Wang, X. Rong, M. Chen, C. Ju, F. Reinhard, H. Chen, J. Wrachtrup, J. Wang, and J. Du, Single-protein spin resonance spectroscopy under ambient conditions, Science **347**, 1135 (2015).

[12] P. Kehayias, A. Jarmola, N. Mosavian, I. Fescenko, F. M. Benito, A. Laraoui, J. Smits, L. Bougas, D. Budker, A. Neumann, S. R. J. Brueck, and V. M. Acosta, Solution nuclear magnetic resonance spectroscopy on a nanostructured diamond chip, Nat. Commun. **8**, 188 (2017).

[13] D. R. Glenn, D. B. Bucher, J. Lee, M. D. Lukin, H. Park, and R. L. Walsworth, High-resolution magnetic resonance spectroscopy using a solid-state spin sensor, Nature **555**, 351 (2018).

[14] D. B. Bucher, D. R. Glenn, H. Park, M. D. Lukin, and R. L. Walsworth, Hyperpolarization-Enhanced NMR Spectroscopy with Femtomole Sensitivity Using Quantum Defects in Diamond, Phys. Rev. X **10**, 021053 (2020).

[15] J. Smits, J. T. Damron, P. Kehayias, A. F. McDowell, N. Mosavian, I. Fescenko, N. Ristoff, A. Laraoui, A. Jarmola, and V. M. Acosta, Two-dimensional nuclear magnetic resonance spectroscopy with a microfluidic diamond quantum sensor, Sci. Adv. **5**, eaaw7895 (2019).

[16] N. Aslam, M. Pfender, P. Neumann, R. Reuter, A. Zappe, F. Fávaro de Oliveira, A. Denisenko, H. Sumiya, S. Onoda, J. Isoya, and J. Wrachtrup, Nanoscale nuclear magnetic resonance with chemical resolution, Science **357**, 67 (2017).

[17] A. O. Sushkov, I. Lovchinsky, N. Chisholm, R. L. Walsworth, H. Park, and M. D. Lukin, Magnetic Resonance Detection of Individual Proton Spins Using Quantum Reporters, Phys. Rev. Lett. **113**, 197601 (2014).

[18] D. Rugar, H. J. Mamin, M. H. Sherwood, M. Kim, C. T. Rettner, K. Ohno, and D. D. Awschalom, Proton magnetic resonance imaging using a nitrogen-vacancy spin sensor, Nat. Nanotechnol. **10**, 120 (2015).

[19] M. Pelliccione, B. A. Myers, L. M. A. Pascal, A. Das, and A. C. Bleszynski Jayich, Two-dimensional Nanoscale Imaging of Gadolinium Spins via Scanning Probe Relaxometry with a Single Spin in Diamond, Phys. Rev. Appl. **2**, 054014 (2014).

[20] A. O. Sushkov, N. Chisholm, I. Lovchinsky, M. Kubo, P. K. Lo, S. D. Bennett, D. Hunger, A. Akimov, R. L. Walsworth, H. Park, and M. D. Lukin, All-optical sensing of a single-molecule electron spin, Nano Lett. **14**, 6443 (2014).

[21] A. Jenkins, S. Baumann, H. Zhou, S. A. Meynell, Y. Daipeng, K. Watanabe, T. Taniguchi, A. Lucas, A. F. Young, and A. C. Bleszynski Jayich, Imaging the Breakdown of Ohmic Transport in Graphene, Phys. Rev. Lett. **129**, 087701 (2022).

[22] F. Casola, T. van der Sar, and A. Yacoby, Probing condensed matter physics with magnetometry based on nitrogen-vacancy centres in diamond, Nat. Rev. Mater. **3**, 17088 (2018).

[23] I. Bertelli, J. J. Carmiggelt, T. Yu, B. G. Simon, C. C. Pothoven, G. E. W. Bauer, Y. M. Blanter, J. Aarts, and T. van der Sar, Magnetic resonance imaging of spin-wave transport and interference in a magnetic insulator, Sci. Adv. **6**, eabd3556 (2020).

[24] T. Lenz, G. Chatzidrosos, Z. Wang, L. Bougas, Y. Dumeige, A. Wickenbrock, N. Kerber, J. Zázvorka, F. Kammerbauer, M. Kläui *et al.*, Imaging Topological

Spin Structures Using Light-Polarization and Magnetic Microscopy, Phys. Rev. Appl. **15**, 024040 (2021).

[25] D. A. Broadway, S. C. Scholten, C. Tan, N. Dontschuk, S. E. Lillie, B. C. Johnson, G. Zheng, Z. Wang, A. R. Oganov, S. Tian, C. Li, H. Lei, L. Wang, L. C. L. Hollenberg, and J.-P. Tetienne, Imaging domain reversal in an ultrathin van der Waals ferromagnet, Advanced Materials **32**, 2003314 (2020).

[26] G. Chatzidrosos, A. Wickenbrock, L. Bougas, N. Leefer, T. Wu, K. Jensen, Y. Dumeige, and D. Budker, Miniature Cavity-Enhanced Diamond Magnetometer, Phys. Rev. Appl. **8**, 044019 (2017).

[27] V. M. Acosta, E. Bauch, A. Jarmola, L. J. Zipp, M. P. Ledbetter, and D. Budker, Broadband magnetometry by infrared-absorption detection of nitrogen-vacancy ensembles in diamond, Appl. Phys. Lett. **97**, 174104 (2010).

[28] E. R. Eisenach, J. F. Barry, M. F. O'Keeffe, J. M. Schloss, M. H. Steinecker, D. R. Englund, and D. A. Braje, Cavity-enhanced microwave readout of a solid-state spin sensor, Nat. Commun. **12**, 1357 (2021).

[29] J. F. Barry, J. M. Schloss, E. Bauch, M. J. Turner, C. A. Hart, L. M. Pham, and R. L. Walsworth, Sensitivity optimization for NV-diamond magnetometry, Rev. Mod. Phys. **92**, 015004 (2020).

[30] D. A. Hopper, H. J. Shulevitz, and L. C. Bassett, Spin readout techniques of the nitrogen-vacancy center in diamond, Micromachines **9**, 437 (2018).

[31] D. F. Jackson Kimball, A. O. Sushkov, and D. Budker, Precessing Ferromagnetic Needle Magnetometer, Phys. Rev. Lett. **116**, 190801 (2016).

[32] E. Bauch, C. A. Hart, J. M. Schloss, M. J. Turner, J. F. Barry, P. Kehayias, S. Singh, and R. L. Walsworth, Ultralong Dephasing Times in Solid-State Spin Ensembles via Quantum Control, Phys. Rev. X **8**, 031025 (2018).

[33] E. Bauch, S. Singh, J. Lee, C. A. Hart, J. M. Schloss, M. J. Turner, J. F. Barry, L. M. Pham, N. Bar-Gill, S. F. Yelin, and R. L. Walsworth, Decoherence of ensembles of nitrogen-vacancy centers in diamond, Phys. Rev. B **102**, 134210 (2020).

[34] M. Balynsky, D. Gutierrez, H. Chiang, A. Kozhevnikov, G. Dudko, Y. Filimonov, A. A. Balandin, and A. Khitun, A magnetometer based on a spin wave interferometer, Sci. Rep. **7**, 11539 (2017).

[35] M. Balinskiy, H. Chiang, A. Kozhevnikov, Y. Filimonov, A. Balandin, and A. Khitun, A spin-wave magnetometer with a positive feedback, J. Magn. Magn. Mater. **514**, 167046 (2020).

[36] C. F. Hempstead, J. T. Sibilia, and J. J. Kostelnick, Precise ferromagnetic resonance magnetometers for differential measurements in fields characterized by large gradients, Rev. Sci. Instrum. **35**, 785 (1964).

[37] K. H. Carpenter and M. K. daSilva, Phase-locked yttrium iron garnet magnetometer for remote measurement of small field changes in a fluctuating background, Rev. Sci. Instrum. **53**, 1414 (1982).

[38] A. Beaumont, M. Buzio, and G. Boero, Ferrimagnetic resonance field sensors for particle accelerators, Rev. Sci. Instrum. **90**, 065005 (2019).

[39] M. Inoue, A. Baryshev, H. Takagi, P. B. Lim, K. Hatafuku, J. Noda, and K. Togo, Investigating the use of magnonic crystals as extremely sensitive magnetic field sensors at room temperature, Appl. Phys. Lett. **98**, 132511 (2011).

[40] A. Kaya, S. Atalay, H. Gencer, O. Kaya, V. Kolat, and T. Izgi, YIG film for magnetic field sensor, Acta Phys. Pol., A **127**, 937 (2015).

[41] T. Koda, S. Muroga, and Y. Endo, Highly sensitive magnetic field sensing using magnetization dynamics in yttrium iron garnet single-crystal thin films, IEEE Trans. Magn. **55**, 1 (2019).

[42] T. Wen, Z. Wang, Q. Du, W. Su, M. Guan, S. Zhao, J. Wu, Z. Hu, Z. Zhou, and M. Liu, Ferromagnetic resonance vector magnetic sensor with high sensitivity and ultra-wide working range, Adv. Mater. Technol. **7**, 2100919 (2022).

[43] N. Koshev, A. Butorina, E. Skidchenko, A. Kuzmichev, A. Ossadtchi, M. Ostras, M. Fedorov, and P. Vetoshko, Evolution of MEG: A first MEG-feasible fluxgate magnetometer, Hum. Brain Mapp. **42**, 4844 (2021).

[44] P. M. Vetoshko, M. V. Valeiko, and P. I. Nikitin, Epitaxial yttrium iron garnet film as an active medium of an even-harmonic magnetic field transducer, Sens. Actuators A: Phys. **106**, 270 (2003).

[45] P. M. Vetoshko, N. A. Gusev, D. A. Chepurnova, E. V. Samoilova, I. I. Syvorotka, I. M. Syvorotka, A. K. Zvezdin, A. A. Korotaeva, and V. I. Belotelov, Flux-gate magnetic field sensor based on yttrium iron garnet films for magnetocardiography investigations, Tech. Phys. Lett. **42**, 860 (2016).

[46] G. Doriath, R. Gaudry, and P. Hartemann, A sensitive and compact magnetometer using Faraday effect in YIG waveguide, J. Appl. Phys. **53**, 8263 (1982).

[47] C. Holthaus, I. Nistor, I. D. Mayergoyz, and C. Krafft, Magnetic-field sensors based on iron garnets with in-plane magnetization, J. Appl. Phys. **99**, 08B308 (2006).

[48] P. Carter, Magnetically-tunable microwave filters using single-crystal yttrium-iron-garnet resonators, IRE Trans. Microw. Theory Tech. **9**, 252 (1961).

[49] R. W. DeGrasse, Low loss gyromagnetic coupling through single crystal garnets, J. Appl. Phys. **30**, S155 (1959).

[50] N. Chang, T. Hayamizu, and Y. Matsuo, YIG-tuned Gunn effect oscillator, Proc. IEEE **55**, 1621 (1967).

[51] M. Omori, Octave electronic tuning of a CW Gunn diode using a YIG sphere, Proc. IEEE **57**, 97 (1969).

[52] P. Ollivier, Microwave YIG-tuned transistor oscillator amplifier design: Application to C band, IEEE J. Solid-State Circuits **7**, 54 (1972).

[53] We note that Balinskiy *et al*. [35] incorporate positive feedback in an oscillator configuration into their magnetometer device, but the positive feedback is only used to enhance the change in observed microwave power depending on the value of magnetic field. The device is not designed to produce sustained oscillations as magnetic fields are varied, nor to measure fields by monitoring the frequency of the circulating microwave power.

[54] C. Kittel, On the theory of ferromagnetic resonance absorption, Phys. Rev. **73**, 155 (1948).

[55] E. van Oort, N. B. Manson, and M. Glasbeek, Optically detected spin coherence of the diamond N-V centre in its triplet ground state, J. Phys. C: Solid State Phys. **21**, 4385 (1988).

[56] J. Dupont-Roc, S. Haroche, and C. Cohen-Tannoudji, Detection of very weak magnetic fields (10^{-9} gauss) by ^{87}Rb zero-field level crossing resonances, Phys. Lett. A **28**, 638 (1969).

[57] N. Crescini, C. Braggio, G. Carugno, A. Ortolan, and G. Ruoso, Cavity magnon polariton based precision magnetometry, Appl. Phys. Lett. **117**, 144001 (2020).

[58] N. F. Ramsey, A molecular beam resonance method with separated oscillating fields, Phys. Rev. **78**, 695 (1950).

[59] A. Dréau, M. Lesik, L. Rondin, P. Spinicelli, O. Arcizet, J.-F. Roch, and V. Jacques, Avoiding power broadening in optically detected magnetic resonance of single NV defects for enhanced dc magnetic field sensitivity, Phys. Rev. B **84**, 195204 (2011).

[60] E. Rubiola, *Phase Noise and Frequency Stability in Oscillators* (Cambridge University Press, Cambridge, UK, 2009).

[61] M. Limes, E. Foley, T. Kornack, S. Caliga, S. McBride, A. Braun, W. Lee, V. Lucivero, and M. Romalis, Portable Magnetometry for Detection of Biomagnetism in Ambient Environments, Phys. Rev. Appl. **14**, 011002 (2020).

[62] W. P. Robins, *Phase Noise in Signal Sources* (Institution of Engineering and Technology, London, UK, 1984).

[63] J. Everard, M. Xu, and S. Bale, Simplified phase noise model for negative-resistance oscillators and a comparison with feedback oscillator models, IEEE Trans. Ultrason. Ferroelectr. Freq. Control **59**, 382 (2012).

[64] R. Rhea, *Discrete Oscillator Design: Linear, Nonlinear, Transient, and Noise Domains*, Artech House microwave library (Artech House, 2010).

[65] R. Boudot and E. Rubiola, Phase noise in RF and microwave amplifiers, IEEE Trans. Ultrason. Ferroelectr. Freq. Control **59**, 2613 (2012).

[66] See Supplemental Material at http://link.aps.org/supplemental/10.1103/PhysRevApplied.19.044044 for additional details of the oscillator phase noise, YIG properties, crystal anisotropy, *S*-parameters for YIG transmission filter, oscillator magnetometer theory of operation, magnetometer noise, intrinsic linewidth measurement, magnetization tip angle, demodulation (magnetic field recovery), and test field calibration, which also includes Refs. [113–143].

[67] I. Kolokolov, V. L'vov, and V. Cherepanov, Magnon interaction and relaxation in yttrium iron garnet, a twenty-sublattice ferromagnet, Sov. Phys. JETP **59**, 1131 (1984).

[68] Y. Tabuchi, S. Ishino, T. Ishikawa, R. Yamazaki, K. Usami, and Y. Nakamura, Hybridizing Ferromagnetic Magnons and Microwave Photons in the Quantum Limit, Phys. Rev. Lett. **113**, 083603 (2014).

[69] M. Goryachev, W. G. Farr, D. L. Creedon, Y. Fan, M. Kostylev, and M. E. Tobar, High-Cooperativity Cavity QED with Magnons at Microwave Frequencies, Phys. Rev. Appl. **2**, 054002 (2014).

[70] X. Zhang, C.-L. Zou, L. Jiang, and H. X. Tang, Strongly Coupled Magnons and Cavity Microwave Photons, Phys. Rev. Lett. **113**, 156401 (2014).

[71] J. Bourhill, N. Kostylev, M. Goryachev, D. L. Creedon, and M. E. Tobar, Ultrahigh cooperativity interactions between magnons and resonant photons in a YIG sphere, Phys. Rev. B **93**, 144420 (2016).

[72] G. Flower, M. Goryachev, J. Bourhill, and M. E. Tobar, Experimental implementations of cavity-magnon systems: From ultra strong coupling to applications in precision measurement, New J. Phys. **21**, 095004 (2019).

[73] D. D. Awschalom *et al.*, Quantum engineering with hybrid magnonic systems and materials, IEEE Trans. Quantum Eng. **2**, 1 (2021).

[74] X. Zhang, C.-L. Zou, L. Jiang, and H. X. Tang, Cavity magnomechanics, Sci. Adv. **2**, e1501286 (2016).

[75] J. Li, S.-Y. Zhu, and G. S. Agarwal, Magnon-Photon-Phonon Entanglement in Cavity Magnomechanics, Phys. Rev. Lett. **121**, 203601 (2018).

[76] S. P. Wolski, D. Lachance-Quirion, Y. Tabuchi, S. Kono, A. Noguchi, K. Usami, and Y. Nakamura, Dissipation-Based Quantum Sensing of Magnons with a Superconducting Qubit, Phys. Rev. Lett. **125**, 117701 (2020).

[77] D. Lachance-Quirion, Y. Tabuchi, S. Ishino, A. Noguchi, T. Ishikawa, R. Yamazaki, and Y. Nakamura, Resolving quanta of collective spin excitations in a millimeter-sized ferromagnet, Sci. Adv. **3**, e1603150 (2017).

[78] J. A. Osborn, Demagnetizing factors of the general ellipsoid, Phys. Rev. **67**, 351 (1945).

[79] B. Lax and K. Button, *Microwave Ferrites and Ferrimagnetics* (McGraw-Hill, New York, NY, USA, 1962).

[80] Micro Lambda Wireless, Inc., Electromagnetic YIG oscillators (2022), https://www.microlambdawireless.com/components/wide-tuning-range-oscillators/.

[81] Teledyne Microwave Solutions, Tiny YIG oscillators (2022), https://www.mrc-gigacomp.com/pdfs/Teledyne-YIG-Products-2014.pdf.

[82] M. L. Korber and E. F. Richardson, A 3.67 GHz permanent magnet, biased YIG-tuned fundamental feedback oscillator, Microw. J. **36**, 104 (1993).

[83] A. A. Sweet and R. Parrott, in *2006 IEEE MTT-S International Microwave Symposium Digest* (IEEE, San Francisco, CA, USA, 2006), p. 581.

[84] A. A. Sweet and R. Parrott, in *2006 European Microwave Integrated Circuits Conference* (IEEE, Manchester, UK, 2006), p. 176.

[85] A. A. Sweet and R. Parrott, in *WAMICON 2014* (IEEE, Tampa, FL, USA, 2014), p. 1.

[86] M. van Delden, N. Pohl, K. Aufinger, C. Baer, and T. Musch, A low-noise transmission-type yttrium iron garnet tuned oscillator based on a SiGe MMIC and bond-coupling operating up to 48 GHz, IEEE Trans. Microw. Theory Tech. **67**, 3973 (2019).

[87] IEEE standard definitions of physical quantities for fundamental frequency and time metrology–random instabilities, IEEE Std 1139-2008 (Revision of IEEE Std 1139-1999), 1 (2009).

[88] M. W. Mitchell and S. Palacios Alvarez, Colloquium: Quantum limits to the energy resolution of magnetic field sensors, Rev. Mod. Phys. **92**, 021001 (2020).

[89] T. Wolf, P. Neumann, K. Nakamura, H. Sumiya, T. Ohshima, J. Isoya, and J. Wrachtrup, Subpicotesla Diamond Magnetometry, Phys. Rev. X **5**, 041001 (2015).

[90] I. Fescenko, A. Jarmola, I. Savukov, P. Kehayias, J. Smits, J. Damron, N. Ristoff, N. Mosavian, and V. M. Acosta, Diamond magnetometer enhanced by ferrite flux concentrators, Phys. Rev. Res. **2**, 023394 (2020).

[91] J. M. Schloss, J. F. Barry, M. J. Turner, and R. L. Walsworth, Simultaneous Broadband Vector Magnetometry Using Solid-State Spins, Phys. Rev. Appl. **10**, 034044 (2018).

[92] R. Wilcox, E. Eisenach, J. Barry, M. Steinecker, M. O'Keeffe, D. Englund, and D. Braje, Thermally Polarized Solid-State Spin Sensor, Phys. Rev. Appl. **17**, 044004 (2022).

[93] J. Krupka, A. Pacewicz, B. Salski, and P. Kopyt, Electrodynamic theory of ferromagnetic resonance and its applications in precise measurements of ferromagnetic linewidth, permeability tensor and saturation magnetization, AIP Adv. **10**, 015018 (2020).

[94] H. Suhl, The nonlinear behavior of ferrites at high microwave signal levels, Proc. IRE **44**, 1270 (1956).

[95] R. V. Pound, Electronic frequency stabilization of microwave oscillators, Rev. Sci. Instrum. **17**, 490 (1946).

[96] R. W. P. Drever, J. L. Hall, F. V. Kowalski, J. Hough, G. M. Ford, A. J. Munley, and H. Ward, Laser phase and frequency stabilization using an optical resonator, Appl. Phys. B **31**, 97 (1983).

[97] Z. Galani, M. J. Bianchini, R. C. Waterman, R. Dibiase, R. W. Laton, and J. B. Cole, Analysis and design of a single-resonator GaAs FET oscillator with noise degeneration, IEEE Trans. Microw. Theory Tech. **32**, 1556 (1984).

[98] C. R. Locke, E. N. Ivanov, J. G. Hartnett, P. L. Stanwix, and M. E. Tobar, Design techniques and noise properties of ultrastable cryogenically cooled sapphire-dielectric resonator oscillators, Rev. Sci. Instrum. **79**, 051301 (2008).

[99] C. Fluhr, S. Grop, B. Dubois, Y. Kersalé, E. Rubiola, and V. Giordano, Characterization of the individual short-term frequency stability of cryogenic sapphire oscillators at the 10^{-16} level, IEEE Trans. Ultrason. Ferroelectr. Freq. Control **63**, 915 (2016).

[100] E. N. Ivanov, M. E. Tobar, and R. A. Woode, Ultra-low-noise microwave oscillator with advanced phase noise suppression system, IEEE Microw. Guided Wave Lett. **6**, 312 (1996).

[101] E. N. Ivanov, M. E. Tobar, and R. A. Woode, Applications of interferometric signal processing to phase-noise reduction in microwave oscillators, IEEE Trans. Microw. Theory Tech. **46**, 1537 (1998).

[102] E. N. Ivanov and M. E. Tobar, Low phase-noise microwave oscillators with interferometric signal processing, IEEE Trans. Microw. Theory Tech. **54**, 3284 (2006).

[103] E. N. Ivanov and M. E. Tobar, Low phase-noise sapphire crystal microwave oscillators: Current status, IEEE Trans. Ultrason. Ferroelectr. Freq. Control **56**, 263 (2009).

[104] E. Rubiola and V. Giordano, Advanced interferometric phase and amplitude noise measurements, Rev. Sci. Instrum. **73**, 2445 (2002).

[105] A. S. Gupta, D. A. Howe, C. Nelson, A. Hati, F. L. Walls, and J. F. Nava, High spectral purity microwave oscillator: Design using conventional air-dielectric cavity, IEEE Trans. Ultrason. Ferroelectr. Freq. Control **51**, 1225 (2004).

[106] F. L. Walls, E. S. Ferre-Pikal, and S. R. Jefferts, Origin of 1/f PM and AM noise in bipolar junction transistor amplifiers, IEEE Trans. Ultrason. Ferroelectr. Freq. Control **44**, 326 (1997).

[107] E. S. Ferre-Pikal, F. L. Walls, and C. W. Nelson, Guidelines for designing BJT amplifiers with low 1/f AM and PM noise, IEEE Trans. Ultrason. Ferroelectr. Freq. Control **44**, 335 (1997).

[108] J. Michl, J. Steiner, A. Denisenko, A. Bülau, A. Zimmermann, K. Nakamura, H. Sumiya, S. Onoda, P. Neumann, J. Isoya *et al*., Robust and accurate electric field sensing with solid state spin ensembles, Nano Lett. **19**, 4904 (2019).

[109] E. H. Chen, H. A. Clevenson, K. A. Johnson, L. M. Pham, D. R. Englund, P. R. Hemmer, and D. A. Braje, High-sensitivity spin-based electrometry with an ensemble of nitrogen-vacancy centers in diamond, Phys. Rev. A **95**, 053417 (2017).

[110] M. Block, B. Kobrin, A. Jarmola, S. Hsieh, C. Zu, N. Figueroa, V. Acosta, J. Minguzzi, J. Maze, D. Budker, and N. Yao, Optically Enhanced Electric Field Sensing Using Nitrogen-Vacancy Ensembles, Phys. Rev. Appl. **16**, 024024 (2021).

[111] G. Kucsko, P. C. Maurer, N. Y. Yao, M. Kubo, H. J. Noh, P. K. Lo, H. Park, and M. D. Lukin, Nanometre-scale thermometry in a living cell, Nature **500**, 54 (2013).

[112] S. Hsieh, P. Bhattacharyya, C. Zu, T. Mittiga, T. J. Smart, F. Machado, B. Kobrin, T. O. Höhn, N. Z. Rui, M. Kamrani, S. Chatterjee, S. Choi, M. Zaletel, V. V. Struzhkin, J. E. Moore, V. I. Levitas, R. Jeanloz, and N. Y. Yao, Imaging stress and magnetism at high pressures using a nanoscale quantum sensor, Science **366**, 1349 (2019).

[113] D. Stancil and A. Prabhakar, *Spin Waves: Theory and Applications* (Springer US, New York, NY, USA, 2009).

[114] E. E. Anderson, Molecular field model and the magnetization of YIG, Phys. Rev. **134**, A1581 (1964).

[115] I. K. Kominis, T. W. Kornack, J. C. Allred, and M. V. Romalis, A subfemtotesla multichannel atomic magnetometer, Nature **422**, 596 (2003).

[116] R. C. LeCraw, E. G. Spencer, and C. S. Porter, Ferromagnetic resonance line width in yttrium iron garnet single crystals, Phys. Rev. **110**, 1311 (1958).

[117] P. Roschmann, Annealing effects on FMR linewidth in Ga substituted YIG, IEEE Trans. Magn. **17**, 2973 (1981).

[118] A. Pacewicz, J. Krupka, B. Salski, P. Aleshkevych, and P. Kopyt, Rigorous broadband study of the intrinsic ferromagnetic linewidth of monocrystalline garnet spheres, Sci. Rep. **9**, 9434 (2019).

[119] R. C. LeCraw and E. G. Spencer, Surface-independent spin-wave relaxation in ferromagnetic resonance of yttrium iron garnet, J. Appl. Phys. **30**, S185 (1959).

[120] J. Helszajn, *YIG Resonators and Filters* (John Wiley & Sons, Chichester, NY, USA, 1985).

[121] P. S. Carter, Side-wall-coupled, strip-transmission-line magnetically tunable filters employing ferrimagnetic YIG resonators, IEEE Trans. Microw. Theory Tech. **13**, 306 (1965).

[122] H. Tanbakuchi, in *1987 17th European Microwave Conference* (IEEE, Rome, Italy, 1987), p. 482.

[123] C. G. Montgomery, R. H. Dicke, and E. M. Purcell, eds., *Principles of Microwave Circuits*, Electromagnetic Waves (Institution of Engineering and Technology, 1987).

[124] Since the oscillating voltage at any point in the oscillator loop has a fixed phase relative to the magnetization, we

do not distinguish between the phase of the magnetization and the phase of the oscillator's voltage output.

[125] A. Cuyt, V. B. Petersen, B. Verdonk, H. Waadeland, and W. B. Jones, *Handbook of Continued Fractions for Special Functions* (Springer Dordrecht, Dordrecht, Netherlands, 2008).

[126] A. Gronefeld, Ultra-low phase noise oscillators with attosecond jitter, Microw. J. **61**, 58 (2018).

[127] D. B. Leeson, A simple model of feedback oscillator noise spectrum, Proc. IEEE **54**, 329 (1966).

[128] P. Schreier and L. Scharf, *Statistical Signal Processing of Complex-Valued Data: The Theory of Improper and Noncircular Signals* (Cambridge University Press, Cambridge, UK, 2010).

[129] R. Tokheim and G. Johnson, Optimum thermal compensation axes in YIG and GaYIG ferrimagnetic spheres, IEEE Trans. Magn. **7**, 267 (1971).

[130] W. A. Yager, J. K. Galt, F. R. Merritt, and E. A. Wood, Ferromagnetic resonance in nickel ferrite, Phys. Rev. **80**, 744 (1950).

[131] J. I. Masters, Instability of magnetic resonance in single crystal spheres of yttrium iron garnet, J. Appl. Phys. **31**, S41 (1960).

[132] J. Clark, J. Brown, and D. E. Tribby, Temperature stabilization of gyromagnetic couplers (correspondence), IEEE Trans. Microw. Theory Tech. **11**, 447 (1963).

[133] D. J. Craik, *Magnetic Oxides* (John Wiley & Sons, New York, NY, USA, 1975).

[134] P. W. Anderson and H. Suhl, Instability in the motion of ferromagnets at high microwave power levels, Phys. Rev. **100**, 1788 (1955).

[135] D. Budker and M. Romalis, Optical magnetometry, Nat. Phys. **3**, 227 (2007).

[136] D. Budker and M. G. Kozlov, Sensing: Equation one, arXiv:2011.11043 (2020).

[137] S. F. Huelga, C. Macchiavello, T. Pellizzari, A. K. Ekert, M. B. Plenio, and J. I. Cirac, Improvement of Frequency Standards with Quantum Entanglement, Phys. Rev. Lett. **79**, 3865 (1997).

[138] W. F. Brown, Thermal fluctuations of a single-domain particle, Phys. Rev. **130**, 1677 (1963).

[139] N. Smith, Fluctuation dissipation considerations for phenomenological damping models for ferromagnetic thin films, J. Appl. Phys. **92**, 3877 (2002).

[140] N. Smith, Modeling of thermal magnetization fluctuations in thin-film magnetic devices, J. Appl. Phys. **90**, 5768 (2001).

[141] N. Smith, Comment on "Fluctuation-dissipation considerations and damping models for ferromagnetic materials", Phys. Rev. B **74**, 026401 (2006).

[142] N. Smith and P. Arnett, White-noise magnetization fluctuations in magnetoresistive heads, Appl. Phys. Lett. **78**, 1448 (2001).

[143] V. L. Safonov and H. N. Bertram, Fluctuation-dissipation considerations and damping models for ferromagnetic materials, Phys. Rev. B **71**, 224402 (2005).